

# Two-Dimensional Magnetic Nozzle Acceleration of a Two-Electron Component Plasma

M. Merino-Martínez\*, E. Ahedo†  
Universidad Politécnica de Madrid, Madrid, Spain

Space Propulsion Conference 2010, May 3 – 6, San Sebastián (Spain)

## Abstract

The influence of a bi-modal Electron Energy Distribution Function consisting on hot and cold electron populations on the expansion of a current-free plasma through a divergent magnetic nozzle is analyzed. Two different models, 1D and 2D, are employed to characterize the plasma response and the formation of potential steepenings, which may bring notable benefits to propulsive applications.

Main results consist on: 1D and 2D plasma property profiles along the nozzle, for the complete quasineutral expansion regime; an analysis of quasineutral profile steepening and double layer formation in terms of the electron population parameters; the 2D structure of these flow features; and a study of the thrust, specific impulse, and plume efficiency provided by the nozzle.

**Key words:** Magnetic Nozzle, Multi-species Plasma, Quasineutral Steepening Layer, Current-Free Double Layer, Propulsive Performances.

## 1 Introduction

Magnetic nozzles constitute one of the most promising accelerating devices for space plasma thrusters. These nozzles consist on a strong convergent-divergent magnetic field, which guides the plasma produced in the chamber and accelerates it into space. During the expansion, the plasma internal energy is employed to accelerate the plasma into a supersonic beam through the self-created ambipolar electric field [1]. In principle, no external electrode is needed to neutralize the current-free beam. The benefits of a magnetic nozzle in improving beam acceleration were shown experimentally by Andersen et al. [2]. The working principle of a magnetic nozzle is somewhat similar to that of the *de Laval* nozzle, wherein a heated neutral gas suffers a sonic transition, expands and accelerates axially, providing thrust. Nevertheless, the fundamental role of the electromagnetic interactions in a magnetic nozzle, and the involved plasma physics, give rise to new phenomena and flow characteristics, not present in the case of a neutral gas expansion.

Some of the most interesting phenomena are due to non-standard Electron Energy Distribution Functions (EEDF), such as the case of two coexisting electron populations of diverse temperature, one cold ( $c$ ) and one hot ( $h$ ).

This type of EEDF may be established during certain ionization and heating processes, such as those of helicon sources. Chen and Hershkowitz [3] have provided evidence of the generation of energetic electron beams in a steady helicon plasma discharge. They showed that the hot beam energy correlates with the wave phase velocity, and suggested electron trapping by the wave as the possible energizing mechanism. Space plasma thrusters based on helicon sources are a subject of current large interest [4, 5, 6], and some research programmes exist to design and develop this type of propulsion systems, such as the Helicon Plasma-Hydrazine combined micro (HPH.com) project [7], which aims to produce a 50 W, dual-mode (hydrazine and plasma) thruster. Expected thruster performance are: 1.5 mN of thrust and a specific impulse  $I_{sp} > 1200$  s. Basically, a helicon-based thruster consists of a cylindrical helicon source where the plasma is produced and heated, and then, it expands and accelerates into the vacuum through a magnetic nozzle.

Charles and Boswell [4] have reported the formation of the aforementioned steepenings near the interphase of a helicon source tube and a larger diffusion chamber, in the form of a Current-Free (CF) Double-Layer (DL). Basically, a double layer consists of a positive and a negative Debye sheath, and connects two quasineutral regions of plasma. Because of its thinness, the double layer is observed as a jump in the profiles of the electric potential and the plasma density. Later, they detected ion beams with a large supersonic velocity (corresponding to a Mach number  $M \simeq 2$ ) [8], which agrees with a potential jump in the double layer, about 3–4 times larger than the plasma temperature in the source. This leads them to suggest the 'double layer helicon thruster' as an innovative and attractive propulsion device.

The current-free double layer is formed only in a limited range of temperature and density ratios of the two electron species [9, 10]. Calling  $\tau$  the hot-to-cold temperature ratio and  $\alpha_0$  the hot-to-total density ratio far upstream, a current-free double layer forms for  $\tau > 10$ , roughly, and a relatively low value of  $\alpha_0$ .

Steepened but fully quasineutral potential profiles are formed for parametric values close to those leading to a double layer formation. To this respect, it is worth to remind that the distinction between a 'quasineutral region' and a 'non-neutral layer' has full sense only in the formal zero Debye length limit, i.e.  $\lambda_D \ll L_c$ , with  $L_c$  the other characteristic length of the problem. This fact is more relevant in the case of the weak current-free double layer where the space-charge fields are not very large.

\*Student, mario.merino@fmetsia.upm.es.

†Professor, eduardo.ahedo@upm.es.

Hairapetian and Stenzel [11] ran an experiment of a collisionless expanding plasma with a controlled population of hot electrons; typical conditions were  $\tau \simeq 20$  and  $\alpha_0 \sim 5\%$ . They demonstrated the direct relation between (a) the presence of a hot electrons and the steepening of the potential profile, and (b) the hot electron temperature and the ion beam energy. The small space-charge relative density ( $\simeq 0.4\%$ ) and the relatively large extension of the steepened region ( $\sim 50\text{--}100$  Debye lengths) illustrates the unclear distinction, in practice, between a weak double layer and a mere steepened quasineutral profile.

The experiment of Hairapetian-Stenzel brings direct evidence that, as long as the plasma is collisionless in the acceleration region, the ion beam energy is determined by the total fall of the electric potential and this depends on the temperature and density of hot electrons. Whether the potential fall is more or less steepened, forming or not a double layer, is marginal for ion acceleration. Therefore, for propulsion applications, it is crucial to determine under which design and operation conditions a helicon-based thruster produces high energy electrons.

The main objective of this work is to fully characterize the acceleration of a three-species plasma through a divergent magnetic nozzle, under the presence of quasineutral profile steepenings caused by the existence of two electron populations with distinct temperatures, with a special focus on the obtained performances for space propulsion. The formation of this steepening and its dependence on the electron population parameters will be covered. A simple 1D model of the plasma acceleration, which was presented in [9, 10], is particularized for our study case. This model makes two basic assumptions that should be well satisfied in an efficient propulsion device. The first one is that the injected neutral gas is fully ionized upstream of the acceleration region. The second one is that for usual plasma parameters, the plasma is almost collisionless in the short acceleration region.

Secondly, the 2D model and the simulation code that we introduced in [12] is extended here to analyze the response of a 3-species plasma. Employing this model and our DiMagNo code — so named after 'Divergent Magnetic Nozzle', — that makes use of the Method of Characteristics (MoC) to reduce and numerically integrate the partial differential equations of the model, we study the radial structure of the plasma expansion and of the quasineutral steepenings. On the basis of these two models, we analyze the influence of the special EEDF on the propulsive performances of the nozzle and on the plume efficiency, which characterizes radial losses.

The rest of the paper is organized as follows: section 2 presents the 1D model, and discusses the formation of the profile steepening under the appropriate conditions. Section 3 describes the 2D model and summarizes the simulation scheme that has been used. In this section, a characterization of the two-dimensional structure of the flow in the nozzle is provided, and some results from the 1D model are extended. Finally, sections 4 and 5 discuss propulsive coefficients and performances, and draw conclusions.

## 2 1D Model of the Plasma Expansion

We shall first consider the expansion of the fully-ionized, collisionless, three-species plasma (constituted of singly-charged cold ions ( $i$ ), and cold ( $c$ ) and hot ( $h$ ) electron populations) through a paraxial nozzle created by a slowly-diverging guide magnetic field. Assuming that  $dR/dz \ll 1$  and that the length hierarchy

$$\lambda_D \ll \ell_e \ll R \ll \lambda_{col} \quad (1)$$

is fulfilled — with  $\ell_e$  the electron gyroradius,  $R$  the nozzle characteristic radius, and  $\lambda_{col}$  the shortest mean-free path of possible collisional processes, — the evolution of the plasma can be adequately described with a one-dimensional, three fluid model. The macroscopic, steady-state equations of the plasma are:

$$\frac{d}{dz} (Ag_i) = 0, \quad (2)$$

$$m_i g_i \frac{d}{dz} (u_i) = -en_i \frac{d\phi}{dz}, \quad (3)$$

$$0 = -\frac{dp_j}{dz} + en_j \frac{d\phi}{dz}, \quad (j = c, h), \quad (4)$$

$$\epsilon_0 \frac{d^2\phi}{dz^2} = e(n_c + n_h - n_i), \quad (5)$$

where:  $g_i = n_i u_i$  is the ion flux,  $A$  the nozzle local area, and other symbols are conventional. Note that ion pressure has been neglected with respect to the coldest electron pressure. We are concerned here with the plasma expansion from the nozzle throat  $S$  (where  $\phi = 0$  has been chosen), to a nozzle end point  $E$ , leaving plasma generation and magnetic detachment outside of our analysis. The EEDF with a hot electron tail will be modeled between these two stations as two distinct isothermal electron species with disparate temperatures  $T_c$  and  $T_h$ . Carrying out the first-integrals of equations 2-4, one has:

$$Ag_i = A_S g_{iS} = G_i = \text{const}, \quad (6)$$

$$\frac{1}{2} m_i u_i^2 + e\phi = \frac{1}{2} m_i u_{iS}^2 = H_i = \text{const}, \quad (7)$$

$$n_j = n_{jS} \exp\left(\frac{e\phi}{T_j}\right), \quad (j = c, h). \quad (8)$$

The small Debye length  $\lambda_D$  limit allows to consider the plasma quasineutral everywhere, and to substitute Eq. 5 with

$$n_i = n_c + n_h = n, \quad (9)$$

except where thin non-neutral layers form — which would appear as discontinuities on the quasineutral scale. The quasineutral plasma satisfying Eq. 9 may be viewed as a single fluid of velocity  $u_i$ , and pressure and (effective) temperature defined by

$$p = T_c n_c + T_h n_h, \quad (10)$$

$$T = \frac{p}{n} = (1 - \alpha) T_c + \alpha T_h, \quad (11)$$

where  $\alpha = n_h/n$  is the local hot-to-total electron density fraction.

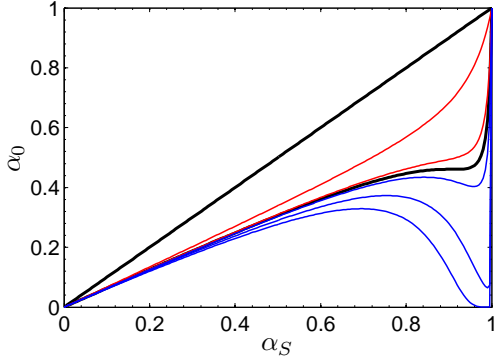


Figure 1: Relation between  $\alpha_0$  and  $\alpha_S$  described by equation 15. This relation becomes the identity function for  $\tau = 1$  (diagonal thick line). There exists a limit value  $\tau^* = 5 + \sqrt{24} \simeq 9.90$  (second thick line), for which the function is univalued if  $\tau \leq \tau^*$ , and multivalued when  $\tau > \tau^*$ . As  $\tau$  increases from 1, the function starts to acquire some curvature (curves in red, for  $\tau = 5, 9$ ). After  $\tau^*$ , there are some  $\alpha_0$  for which three possible  $\alpha_S$  exist ( $\tau = 11, 18, 50$ , in blue), reflecting that three different sonic transitions are possible.

Equations 7 and 8 show that  $u_i$ ,  $n_c$  and  $n_h$  are functions of  $\phi$  only. Hence, so are  $p$ ,  $T$  and  $n$ . The thermodynamic behavior of this one-degree-of-freedom gas is characterized by its specific enthalpy, which coincides with the electrostatic energy,  $dh = dp/n = e d\phi$ . Combining equations 2, 3, 4, 9 and 11, the motion of such fluid is described by the expression

$$\frac{d \ln u_i}{dz} = \frac{1}{(M^2 - 1)} \frac{d \ln A}{dz}, \quad (12)$$

where  $M = u_i/c_s$  is the Mach number based on the (effective) local sound speed of the medium,

$$c_s = \sqrt{\frac{1}{m_i} \frac{dp}{dn}} = \sqrt{\frac{1}{m_i} \frac{n}{(n_h/T_h + n_c/T_c)}} = \sqrt{\frac{\gamma T}{m_i}}, \quad (13)$$

with the (effective) specific heat ratio defined as

$$\gamma = \frac{n}{p} \frac{dp}{dn} = \frac{n^2}{(n_h T_h + n_c T_c) (n_h/T_h + n_c/T_c)}. \quad (14)$$

Parametrically, the three-species plasma expansion is characterized by the temperature ratio  $\tau = T_h/T_c$  and the far upstream electron density ratio (station where  $u_i = 0$ , here denoted with subindex 0),  $\alpha_0 = n_{h0}/n_0$ . Due to its particular interest, and its usefulness below, we also define this ratio at the nozzle throat,  $\alpha_S = n_{hS}/n_S$ . From Eq. 7, imposing that the flow at the throat is sonic, the relation between both parameters is

$$1 + \frac{(1 - \alpha_S)}{\alpha_S} \exp \left[ \frac{\tau - 1}{2(\tau - \tau \alpha_S + \alpha_S)} \right] = \frac{1}{\alpha_0}, \quad (15)$$

which has been plotted in Fig. 1, and is not a univaluated function for every value of  $\tau$ . This is the first indication of the existence of different flow regimes, and the possibility that discontinuities in some flow properties arise in the plasma expansion.

The mathematical expressions of the model can be made dimensionless using  $n_S$  (total electron density at

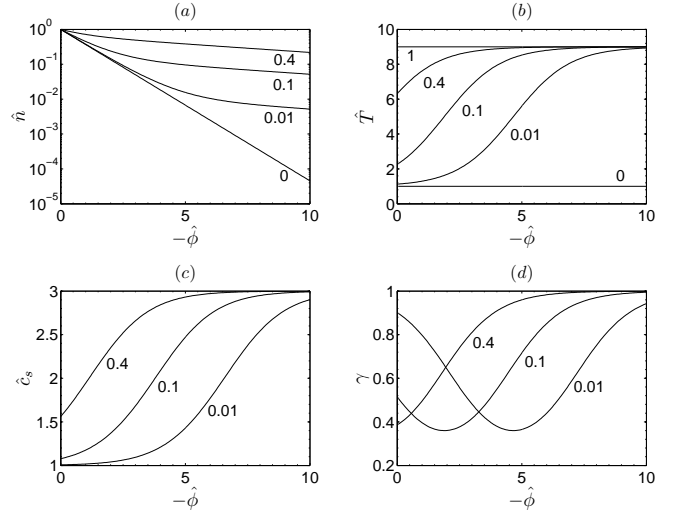


Figure 2: Dependence of the main variables with  $\phi$  for  $\tau = 9$ . Numbers indicate the value of  $\alpha_0$  of each line.

the throat),  $T_c$ ,  $e$ ,  $m_i$ , and  $R_S$  (the nozzle radius at the throat). Dimensionless variables will be distinguished with a hat, i.e.,  $\hat{u}_i = u_i/\sqrt{T_c/m_i}$  for the ion velocity,  $\hat{\phi} = e\phi/T_c$  for the potential, and so on.

The dependence of the main variables on  $\phi$  for various values of  $\tau$ ,  $\alpha_0$  is presented on Fig. 2. Due to the different exponential character of  $n_c$  and  $n_h$ , as the plasma accelerates and  $\phi$  decreases, the density of the colder, lower energy electrons  $n_c$  decreases much faster than  $n_h$ , and hence hot-electron properties dominate far downstream. This explains the shift of  $T$  and  $c_s$  from  $\simeq T_c$  and  $\simeq \sqrt{T_c/m_i}$  to  $\simeq T_h$  and  $\simeq \sqrt{T_h/m_i}$ , respectively, in the range  $0 < -\hat{\phi} < \tau$ . The most outstanding feature is the unusual behavior of  $\gamma$ , which is close to unity when one of the electron species dominates, but presents an intermediate minimum that tends to zero when  $\tau \gg 1$ . According to Eq. 14, the physical meaning of  $\gamma < 1$  is that the gas temperature increases as the gas expands. These anomalous thermodynamics were already pointed out by Bezzerides et al. [13] and are at the core of all the special phenomena that arises in the acceleration of the 3-species plasma, and the formation of profile steepenings and non-neutral layers within the jet.

Combining equations 7 and 8, the dimensionless ion flux in a *quasineutral expansion* can be expressed as follows:

$$\begin{aligned} \hat{g}_i(\hat{\phi}; \tau, \alpha) &= \hat{u}_i \hat{n} = \\ &= \sqrt{2\hat{H}_i - 2\hat{\phi}} \left[ (1 - \alpha_S) e^{\hat{\phi}} + \alpha_S e^{\hat{\phi}/\tau} \right], \end{aligned} \quad (16)$$

where, from the sonic condition at the throat,  $2\hat{H}_i = (1 - \alpha_S + \alpha_S/\tau)^{-1}$ . Together with the continuity equation, Eq. 2, this expression yields an implicit relation for the potential at each section of the magnetic nozzle,

$$\frac{\hat{g}_i(\hat{\phi})}{\hat{g}_{iS}} = \frac{A_S}{A(\hat{z})}. \quad (17)$$

The right-hand-side of 17 presents a maximum at the nozzle throat. Since the plasma accelerates in the direction of the flow, the potential  $\phi$  must monotonically decrease along the nozzle. This monotonicity implies that,

for the plasma evolution to be fully quasineutral,  $\hat{g}_i(\hat{\phi})$  must present one and only one extremum (a maximum) as well. The extrema of this function are given by

$$0 = \frac{d\hat{g}_i}{d\hat{\phi}} = -\frac{1}{\sqrt{2\hat{H}_i - 2\hat{\phi}}} \left[ (1 - \alpha_S) e^{\hat{\phi}} + \alpha_S e^{\hat{\phi}/\tau} \right] + \sqrt{2\hat{H}_i - 2\hat{\phi}} \left[ (1 - \alpha_S) e^{\hat{\phi}} + \frac{\alpha_S}{\tau} e^{\hat{\phi}/\tau} \right]. \quad (18)$$

A detailed analysis of equations 16 and 12 reveals that  $d\hat{g}_i/d\hat{\phi} < 0$  during a subsonic expansion of the plasma,  $d\hat{g}_i/d\hat{\phi} > 0$  for supersonic flow, and  $d\hat{g}_i/d\hat{\phi} = 0$  at the sonic transition. Hence, the solutions of Eq. 18 coincide with sonic transitions  $M = 1$ , and so, one of them must be located at the throat for the magnetic nozzle to function nominally. In previous work by Ahedo and Martínez-Sánchez [9, 10] it was shown that  $\hat{g}_i(\hat{\phi})$  presents one or three local extrema depending on  $\alpha_0$  and  $\tau$ . When  $\tau$  is below the threshold value  $\tau^* = 5 + \sqrt{24} \simeq 9.90$ , there is a single maximum (located at  $\hat{\phi} = 0$ ) for any  $\alpha_0$ . For  $\tau > \tau^*$ , there are two maxima (located at  $\hat{\phi} = 0$  and  $\hat{\phi} \sim \hat{H}_i - \tau/2$ ) and one minimum when  $\alpha_0$  is between two limit curves,  $\alpha_{01}(\tau)$  and  $\alpha_{02}(\tau)$ , which correspond to fulfilling  $d\hat{g}_i/d\hat{\phi} = 0$  and  $d^2\hat{g}_i/d\hat{\phi}^2 = 0$  simultaneously. Physically, plasma on any of these limit curves yields a spatial solution with  $d\hat{\phi}/d\hat{z} = \infty$  at some point in the nozzle — for  $\alpha_{01}$ , this happens in the divergent side, and for  $\alpha_{02}$  in the convergent side, — although  $\hat{\phi}(\hat{g}_i)$  is not multivalued yet. Outside of the region delimited by these curves, the plasma expansion is completely quasineutral. This is in direct correlation with the fact that Eq. 15 is multivalued for  $\tau > \tau^*$  for certain values of  $\alpha_0$ , since the curves given by Eq. 15 reflect all the existing extrema of  $\hat{g}_i(\hat{\phi})$ .

Fig. 3 shows the Mach number as a function of  $\hat{\phi}$ ,  $M(\hat{\phi})$ , which for a three-species plasma is not monotonic and presents a minimum that tends to 1 as the curves  $\alpha_{01}(\tau)$  and  $\alpha_{02}(\tau)$  are approached from the quasineutral regime. For a parametric point inside the region delimited by these curves, this function becomes  $M < 1$  around this minimum. However, Eq. 12 shows that no other regular sonic transition but the one in the nozzle throat can exist, unless  $d \ln u_i/dz \rightarrow \infty$ , and then a discontinuity — or, more precisely, a double layer — takes place. Therefore, the solutions with intermediate discontinuities shown in [9] are announced by the presence of singular/sonic points outside the nozzle throat. In the DL formation regime, a jump of the potential (in the macroscopic scale) exists that connects two branches of  $\hat{\phi}(\hat{g}_i)$ .

The different regimes of the plasma flow are shown in the maps of the parametric planes  $(\tau, \alpha_0)$  and  $(\tau, \alpha_S)$  of Fig. 4. Two extra boundary lines exist,  $\alpha_{03}(\tau)$  and  $\alpha_{04}(\tau)$ , which divide the DL regime into secondary parametric domains, which take into account where the DL forms: in the divergent side of the nozzle [from  $\alpha_{01}(\tau)$  to  $\alpha_{03}(\tau)$ ], at the throat [from  $\alpha_{03}(\tau)$  to  $\alpha_{04}(\tau)$ ], or at the convergent side [from  $\alpha_{04}(\tau)$  to  $\alpha_{02}(\tau)$ ].

We shall focus here on the plasma expansion in the divergent part of the nozzle from  $S$  to  $E$ , and for values of  $\tau$ ,  $\alpha_0$  outside the parametric region delimited by  $\alpha_{01}(\tau)$  and  $\alpha_{02}(\tau)$ , so that  $\hat{g}_i(\hat{\phi})$  has only a single maximum.

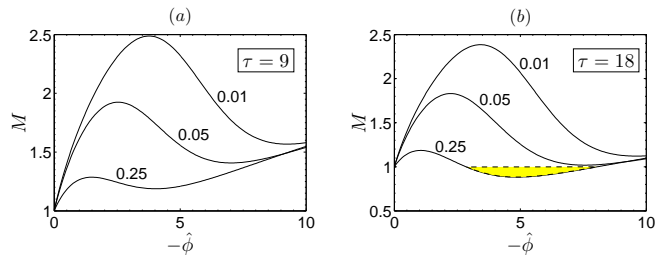


Figure 3: Mach number dependence with  $\phi$  for  $\tau = 9$  (a), slightly below  $\tau^*$ , and  $\tau = 18$  (b). Numbers indicate the value of  $\alpha_0$  of each line. The yellow region of the latter, pointing where  $M < 1$ , indicates the existence of a CDFL for that particular case ( $\alpha_0 = 0.3$ ).

Therefore, the plasma expansion is fully quasineutral, and no macroscopic discontinuities — no double layers — are present. In this region  $\alpha_S$  is a univalued function of  $\alpha_0$ . Even so, the anomalous thermodynamics of the three-species plasma already have profound implications on the development of the jet: as the DL region is approached, a Quasineutral Steepening Layer (QSL) in the potential forms. This QSL ultimately turns into a DL, when  $\tau$  and  $\alpha_0$  enter the DL regime. The distinction between an actual DL and a QSL is however a matter of scale only, and both structures have an almost identical influence on the plasma expansion, being the total potential fall the determinant factor in all cases.

In order to remove the dependence of the solution on the nozzle shape, the spatial-like variable  $\zeta = \sqrt{A/A_S - 1}$  will be used. For instance, the local electric field is measured by

$$\frac{d\phi}{dz} = \frac{d\phi}{d\zeta} \frac{d\zeta}{dz} \quad (19)$$

where the first and second terms on the right-hand side correspond to the influence of the expansion ratio and the precise nozzle shape respectively. The influence of the latter is straightforward, so our attention here is centered exclusively on the spatial dependence on  $\zeta$  contained in the first term.

Fig. 5 and 6 plot the spatial profiles (along  $\zeta$ ) of  $\hat{\phi}$  in terms of  $\alpha_0$ , for  $\tau = 9$  and 18, respectively. In Fig. 5 show that as  $\alpha_0$  increases from zero, a QSL (measured relative to  $\zeta$ ) develops in the potential and other variables. This development takes place mainly at  $\alpha_0$  small (which is the expected practical range), while the maximum QSL for  $\tau = 9$  is reached around  $\alpha_0 \sim 0.3$  (close to the parametric region's boundary), and the plasma profile becomes almost insensitive to  $\alpha_0$  for  $\alpha_0 > 0.5$ , roughly. Interestingly, the QSL for low  $\alpha_0$  ( $\alpha_0 \sim 6\%$ ) are similar in magnitude to the ones for  $\alpha_0 > 0.5$ , when results are considered relative to the plasma temperature at the throat,  $T_S$ . As  $\alpha_0$  increases, the location of the QSL moves from far downstream toward the nozzle throat, but it remains in the divergent side of the nozzle for the main range of interest,  $\alpha_0 < 0.3$ . Note that for the steepening to actually occur, the nozzle expansion area must be large enough — or  $\alpha_0$  large enough — for it to take place before  $\zeta_E$ , the nozzle end section.

The QSL acts as a rather effective barrier for cold electrons, whereas  $n_h$  remains almost constant upstream of

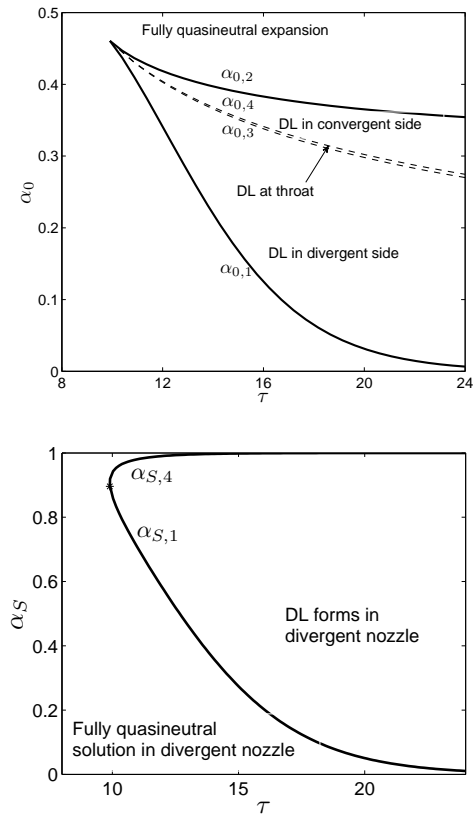


Figure 4: Parametric regimes of the plasma expansion. the limit curves  $\alpha_{01}(\tau)$ ,  $\alpha_{02}(\tau)$ ,  $\alpha_{03}(\tau)$  and  $\alpha_{04}(\tau)$  divide the  $(\tau, \alpha_0)$  and  $(\tau, \alpha_S)$  planes in different regions [10].

the QSL, and dominates the electron population downstream ( $\alpha \rightarrow 1$ ). For this reason, the sound speed makes the transition from the 'cold' to the 'hot' value in the neighborhood of the QSL location as well. Moreover, the maximum ion acceleration, as Fig 5 (d) shows, occurs at the QSL, but in a narrower interval of the nozzle.. This explains why the Mach number presents a minimum at that position and starts to increase at a fast rate afterward.

In the case of  $\tau = 18$ , as  $\alpha_0$  increases, the QSL turns into a DL, the onset being at around  $\alpha_0 \simeq 0.06$  ( $\alpha_S \simeq 0.11$ ). In spite of the discontinuity in the flow properties that the DL poses, there is no practical difference with respect to a QSL as mentioned before, in that the obtained downstream values depend mainly on the total potential fall that takes place in the nozzle.

### 3 Two-dimensional plasma model and simulation

A deeper insight into the plasma expansion in the magnetic nozzle can be gained with a two-dimensional model. In this way, it is possible to study the radial gradients, the shape of the QSL, and evaluate the plume efficiency of the nozzle — i.e., the radial losses of the jet. This also facilitates a more accurate analysis in the case of rapidly-diverging, non paraxial geometries, where the assumption  $dR/dz \ll 1$  of the previous section fails.

The plasma model that we presented in [12, 14, 15] for

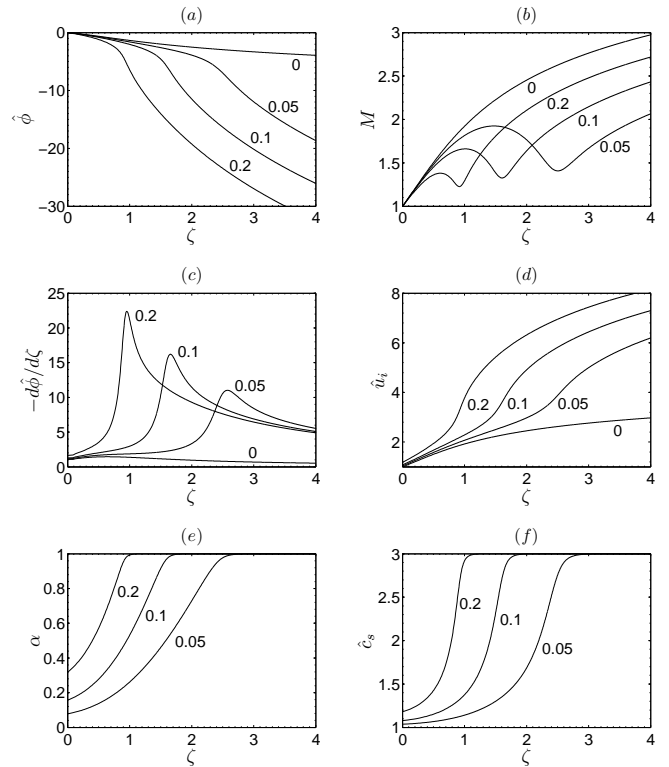


Figure 5: 1D Plasma expansion profiles for  $\tau = 9$ . Numbers beside each line indicate the value of  $\alpha_0$ . End section has been placed at  $\zeta_E = 4$ .

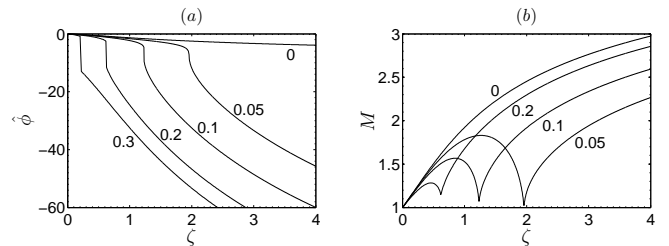


Figure 6: 1D Plasma expansion profiles for  $\tau = 18$ . In this case, the QSL gets steeper until it finally becomes a CFDL, when  $(\alpha_0, \tau)$  is inside the parametric region of double layer formation. Numbers beside each line indicate the value of  $\alpha_0$ . End section has been placed at  $\zeta_E = 4$ .

a two-species plasma has been extended here to include two distinct electron species. The principal aspects of this model can be summarized as follows.

For an axisymmetric nozzle, in which a three-species, low- $\beta$  plasma (defined as  $\beta = 2\mu_0 p/B^2$ , parameter that measures the relative importance of thermal pressure to magnetic pressure) is flowing under the same hypothesis as before (section 2), the equations of the model are:

$$\nabla \cdot n_j \mathbf{u}_j = 0, \quad (j = i, c, h), \quad (20)$$

$$m_i n_i \mathbf{u}_i \cdot \nabla \mathbf{u}_i = -en_i \nabla \phi + en_i \mathbf{u}_i \wedge \mathbf{B}, \quad (21)$$

$$0 = -\nabla p_j + en_j \nabla \phi - en_j u_{\theta j} B \mathbf{1}_{\perp} = 0, \quad (j = c, h), \quad (22)$$

where  $\mathbf{1}_{\perp}$  belongs to the orthonormal base  $\{\mathbf{b} = \mathbf{B}/B, \mathbf{1}_{\perp} = \mathbf{1}_{\theta} \wedge \mathbf{b}, \mathbf{1}_{\theta}\}$ , defined from the local magnetic field. From the length scale hierarchy of Eq. 1, it follows that electrons are completely magnetized — i.e., electron streamtubes (each species) coincide

with magnetic streamtubes. As a consequence, and due to the quasineutrality condition, the last electron streamtube is also the last ion streamtube. Continuity equations (Eq. 20) show that a streamfunction  $\psi_j$  that verifies  $\nabla\psi_j = n_j r \mathbf{1}_\theta \wedge \mathbf{u}_i$  exists for each species in the plasma ( $j = i, c, h$ ). Similarly, there exists a magnetic streamfunction  $\psi_m$  satisfying  $\nabla\psi_m = r \mathbf{1}_\theta \wedge \mathbf{B}$ .

Projecting Eq. 22 along  $\mathbf{b}$  and modeling the electrons again as two isothermal species provides

$$T_j \ln(n_j/n_{jS}) - e\phi = H_j(\psi_m), \quad (j = c, h) \quad (23)$$

(notice that this is similar to Eq. 8, but now  $H_j(\psi_m) \neq 0$ , if the plasma profiles at  $S$  are not uniform). The same equation projected along  $\mathbf{1}_\perp$  yields

$$eu_{\theta j}/r = -dH_e/d\psi_m, \quad (24)$$

which allows to calculate  $u_{\theta j}$ . From this expression it follows that, if  $u_{\theta j}$  is initially zero in our non-collisional plasma, it remains so throughout the expansion. The ion momentum equation (Eq. 21) along  $\mathbf{1}_\theta$  can be integrated to obtain

$$rm_i u_{\theta i} + e\psi = D_i(\psi_i), \quad (25)$$

which states the conservation of ion axial angular momentum. These relations conform a set of algebraic equations that provide  $n_c$ ,  $n_h$ , and  $u_{\theta j}$  ( $j = i, c, h$ ) as functions of  $\phi$ , initial conditions, and the local value of the magnetic field. To obtain the variables,  $u_{zi}$ ,  $u_{ri}$  and  $\phi$ , the method of characteristics [16] is employed to transform the remaining partial differential equations — ion continuity equation, and ion momentum in the  $z$  and  $r$  directions — into the following ordinary differential equations along the Mach lines (denoted as the  $C_+$ ,  $C_-$  curve families) and the ion streamlines ( $C_o$ ):

$$\begin{aligned} u_{ri} \frac{du_{zi}}{dz} \Big|_{C_\pm} - u_{zi} \frac{du_{ri}}{dz} \Big|_{C_\pm} \mp \frac{e}{m_i} \sqrt{M^2 - 1} \frac{d\phi}{dz} \Big|_{C_\pm} = \\ = (u_{ri} - \lambda_\pm u_{zi}) f + \lambda_\pm g - h \end{aligned} \quad (26)$$

$$\frac{d}{dz} \Big|_{C_o} \left( \frac{1}{2} m_i u_i^2 + e\phi \right) = 0 \quad (27)$$

where  $\lambda_\pm = (u_{zi} u_{ri} \pm c_{si} \sqrt{u_{zi}^2 + u_{ri}^2 - c_{si}^2}) / (u_{zi}^2 - c_{si}^2)$  and  $\lambda_o = u_{ri}/u_{zi}$  are the local slopes of the characteristic curves, and

$$f = \sum_{j=c,h} \left( \frac{en_j u_{\theta j}}{nT_j} \right) (u_{ri} B_z - u_{zi} B_r) - \frac{u_r}{r};$$

$$g = -u_{\theta i} \frac{eB_r}{m_i}; \quad h = u_{\theta i} \frac{eB_z}{m_i} + \frac{u_{\theta i}^2}{r}.$$

Notice that Eq. 27 expresses the conservation of ion mechanical energy along streamlines, as did Eq. 7 in the 1D model — and, again, this time the constant  $H_i(\psi_i)$  can vary across streamlines, if initial conditions are not uniform. These equations are integrated numerically with the DiMagNo code that we presented in [12]. Electron continuity equations then provide

$$\frac{n_j u_{\parallel j}}{B} = G_j(\psi_j), \quad (j = c, h), \quad (28)$$

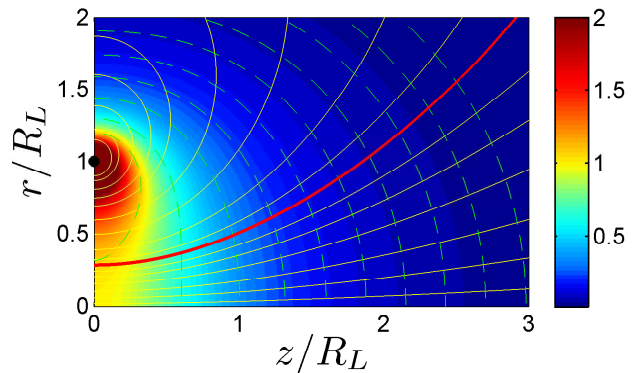


Figure 7: Meridian plane of the magnetic field created by a current loop placed at  $r = R_L$ . Yellow lines are field lines. The line chosen as nozzle outer line has been highlighted in red. Green, dashed lines represent  $B$ -constant lines. The background color shows the magnetic field intensity relative to  $B_S$ , its value at the origin.

that, with a proper boundary condition, yield  $u_{\parallel j}$ , the component of the electron fluid velocity in the meridian plane (parallel to the magnetic field).

Although the model is applicable to any divergent magnetic nozzle, in the following the magnetic circuit is here reduced to a single current loop placed at  $(z, r) = (0, R_L)$ , with an intensity  $I_L$  flowing along  $\mathbf{1}_\theta$ . For such a current loop, the magnetic streamfunction is [17]:

$$\psi_m(z, r) = \frac{2B_S R_L^2 r}{\pi} \cdot \frac{(2 - k^2) \mathbf{K}(k^2) - 2\mathbf{E}(k^2)}{k^2 \sqrt{(R_L + r)^2 + z^2}}, \quad (29)$$

where  $k^2 = 4R_L r [(R_L + r)^2 + z^2]^{-1}$ ,  $B_S = B_z(0, 0) = \mu_0 I_L / (2R_L)$ , and  $\mathbf{K}(m)$  and  $\mathbf{E}(m)$  are the complete elliptic integrals of first and second kind, respectively (with the argument  $m$  defined as in [18]). The dimensionless number  $R_L/R_S$  controls the divergence rate of the nozzle. The condition  $\beta \ll 1$  implies that the magnetic field induced by the plasma internal currents can be neglected with respect to the applied field (at least, in the near-region of the nozzle). Hence, our nozzle's magnetic field geometry coincides with that of the guide field. Fig. 7 presents this magnetic field. The effects of non-uniformities in plasma properties at the nozzle throat and a partial ion magnetization strength, characterized by the field intensity at the origin  $B_S$  — or, more precisely, by the dimensionless ion gyrofrequency,

$$\hat{\Omega}_{iS} = eB_S R_S / (m_i c_{sS}), \quad (30)$$

were already studied in [12]. Main results are the fact that (a) a non-uniform initial condition, (b) weakly magnetized ion flow, and (c) slowly diverging magnetic fields are favorable for propulsive performances. This study also shows that, for non-completely magnetized ions, electron and ion streamtubes do not coincide, and non-negligible electric currents arise inside the nozzle, which imply that the current ambipolarity condition is not met. Hence, we will restrict our analysis here to initially uniform flows and weakly magnetized ions (say,  $\hat{\Omega}_{iS} = 0.1$ ).

Following this scheme, the expansion of an initially uniform plasma at the nozzle throat has been simulated

for different values of  $\tau$  and  $\alpha_S$ . Since the ion flow must be supersonic in order to apply the MoC, an initial value of the Mach number at the nozzle throat slightly higher than 1 ( $M_S = 1.05$ ) has been used, after checking numerically that the solution is almost insensitive to  $M_S$  when  $M_S - 1 \ll 1$ .

Fig. 8 covers a number of cases with  $\tau = 9$ . In these graphs, the different variables have been referred to the *average electron temperature* at the origin,

$$T_S = (1 - \alpha_S)T_c + \alpha_S T_h, \quad (31)$$

that allows to compare the behavior of each plasma in equal grounds, in terms of their internal energy at the throat. Notice also that we now use  $\alpha_S$  instead of  $\alpha_0$ , as it is more representative of the plasma composition at the entrance of the divergent part of the nozzle. This shows an interesting increase in the total potential fall between sections  $S$  and  $E$  for three-species plasma.

As it can be seen, a mild QSL forms at different positions in the nozzle, and it moves toward the throat as  $\alpha_S$  increases. The radially-averaged expansion profiles agree well with the 1D model. Also in agreement with the 1D model, the Mach number decreases and reaches a minimum around this spot. A new aspect of the expansion, revealed by the 2D model, is that the minimum Mach number is reached first on the outer streamline than on the axis. Actual ion velocity is always monotonic, but presents large differences between its value on the outer and inner lines, specially around the QSL. This difference decreases after this steepening, to start increasing slowly afterward. The fact that  $u_i/\sqrt{T_S/m_i}$  is larger in the simulation with  $\alpha_S = 0.2$  (blue) than in the one with  $\alpha_S = 0.1$  (red) in spite of the nearly equal final potential  $\hat{\phi}$  is due to the role of the specific heat ratio function,  $\gamma$ . From Eq. 27 (or the integrated version for initially uniform plasma flow, Eq. 7):  $u_i^2/(T_S/m_i) = 1 - 2e\phi/(T_S\gamma)$ .

Fig. 8 (c) shows that downstream the QSL the potential at the exterior line falls at a higher rate than at the center line. This potential difference translates into a radial electric field that accelerates ions, adding to the radial losses. The QSL has a maximum  $E_z$  electric field on the axis at roughly  $\alpha_S = 55\%$  when measured relative to  $T_c$ , and at low  $\alpha_S$  relative to  $T_S$ . However, this larger maximum of the electric field for low  $\alpha_S$  takes place always further downstream as  $\alpha_S$  is decreased, revealing the necessity to operate with ever larger magnetic nozzles — and therefore ever stronger magnetic fields — to take advantage of this flow phenomenon. Therefore, for propulsion applications, where the objective is to deliver maximal thrust at minimum weight, it may be interesting to position the QSL closer to the nozzle throat, so ions are earlier accelerated by this structure.

Analogously, Fig. 9 presents the results for  $\tau = 18$ . In this case, as we are approaching the limit line  $\alpha_{S1}(\tau)$ , the Mach number at the steepening point decreases rapidly to 1. The simulation with  $\alpha_S = 0.09$  presents a very sharp minimum of  $M$  on both the outer and center streamlines, which for  $\alpha_{S1}$  would actually become an angular point. On this line and beyond, the existence of a secondary sonic transition turns the system of equations parabolic at that position, and the integration with the MoC fails. At any rate, the cases of actual interest are those where the hot-to-total electron density ratio

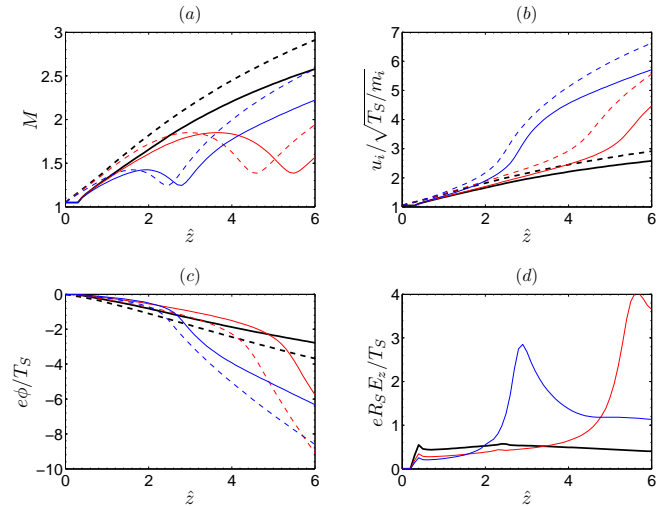


Figure 8: 2D plasma expansion profiles with  $\tau = 9$ . Various simulations with different  $\alpha_S$  have been plotted: thick lines represent the reference, two-species plasma ( $\alpha_S = 0$  or  $\alpha_S = 100$ , which coincide since results are referred to  $T_S$ ). Red lines show  $\alpha_S = 0.1$ , and blue lines  $\alpha_S = 0.2$ . Values at the center line are in solid lines. Dashed lines refer to the exterior streamline. End section,  $\hat{z}_E = 6$ , has  $R_E \simeq 3.15$ , which translates into  $\zeta_E = 3$ .

is small, say  $\alpha_S < 0.1$ . Ion velocity differences between both streamlines in the neighborhood of the QSL become much larger for  $\tau = 18$  than for  $\tau = 9$ . Interestingly, the potential along these streamlines does not diverge as much as for  $\tau = 9$  after the steepening. The maximum electric field on the axis is very acute, and would become infinite when the CFDL discontinuity develops.

As it can be seen in Figs. 8 and 9, the evolution of the plasma along the axis line and the outer streamline is similar for each variable, but the position of the QSL on the outer one occurs slightly before than on the center one. This reveals the 2D structure of this flow feature, which can be better appreciated in Fig. 10. While potential isolines possess a near-parabolic shape, with a curvature that increases further downstream (note however that in the  $\tau = 18$  case this shape becomes slightly more complicated downstream of the QSL), the geometry of the region of maximum electric field,  $eR_S E/T_S$ , does not exactly coincide with these lines, and presents a slightly different shape. This is due to the fact that  $\phi$ -isolines are less spaced at the outer streamline than at the axis, because of their increasing curvature. This shows that radial differences exist that affect the way ions are accelerated.

Since  $m_i u_i^2/2 + e\phi = H_i(\psi_i)$  and the plasma is initially uniform,  $u_i$  isolines coincide with  $\phi$  isolines — and, for analogous reasons, so do the isolines of  $n_c$ ,  $n_h$ ,  $\gamma$ ,  $M$  and other variables. Hence, most of the relevant information about the plasma expansion is already provided by the 1D model, when constant- $\phi$  lines are considered. However, the ion velocity field is not totally determined unless both  $u_{zi}$ ,  $u_{ri}$  are locally known. The non-zero value of  $u_{ri}$  has a direct influence on the plume efficiency that will be defined in next section, as it signifies radial losses. Notice that, in the cases of interest where ions

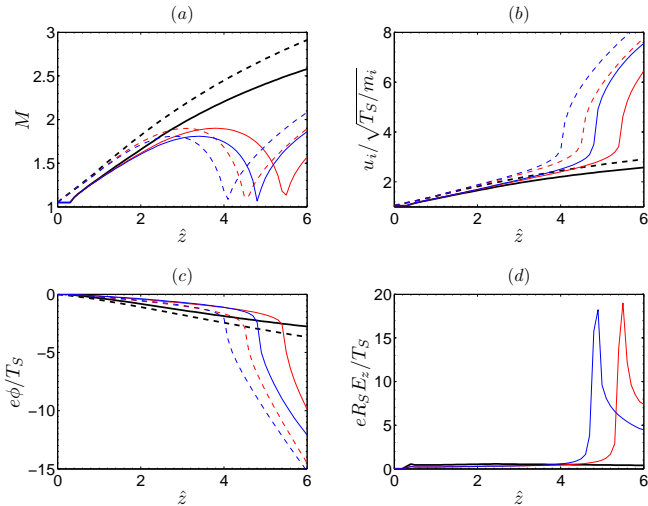


Figure 9: 2D plasma expansion profiles with  $\tau = 18$ . Similarly to the previous figure, thick lines are for the reference, two-species plasma ( $\alpha_S = 0$  or  $\alpha_S = 100$ ). Red lines show  $\alpha_S = 0.07$ , and blue lines  $\alpha_S = 0.09$ , very close to the limit line  $\alpha_{S1}(\tau)$  of CFDL formation. Values at the center line are in solid lines. Dashed lines refer to the exterior streamline. Again end section is located at  $\hat{z}_E = 6$ , with  $R_E \simeq 3.15$ .

are not completely magnetized, the two velocity components cannot trivially known, and a 2D model becomes necessary to evaluate these properties.

## 4 Propulsive performances of the three-species plasma

After fully characterizing the plasma expansion in the quasineutral parametric region with both the 1D and 2D models, we now turn our attention to the influence of the hot electron tail on the propulsive parameters of the nozzle. Although our plasma model can estimate the propulsive gains and the radial losses, it cannot provide information on the global efficiencies of the device. This would require matching with (a) the upstream process of plasma ionization and heating, and (b) the modeling of the magnetic detachment far downstream, which is out of the scope of the present work.

The main parameters of interest that describe the potential of the system as an accelerating device are the produced thrust  $F_E$ , the specific impulse  $I_{sp} = F_E / (m_i g_i)$  (here in velocity units), and the plume efficiency  $\eta_{plume}$ . Since  $I_{sp}$  is the effective plasma velocity at the nozzle exhaust, its increment with respect to ion velocity at the entrance is approximately proportional to the square root of the total potential fall between stations  $S$  and  $E$ :  $I_{sp} \propto \sqrt{2e(\phi_S - \phi_E) / m_i}$ . A first measure of the energy spent on the plasma in the thruster chamber is the average electron temperature at the origin,  $T_S$ . Therefore, for propulsion applications it is of great interest to analyze the potential fall obtained for different  $\tau$ ,  $\alpha_S$ , relative to this temperature. This fall was shown in Figs. 8 and 9, and is presented at  $R_E = 3.15$  as a function of  $\alpha_S$  on Fig. 12 (a). As it can be seen, a small fraction of hot electrons ( $\alpha_S \simeq 0.1$ ) can more than trip-

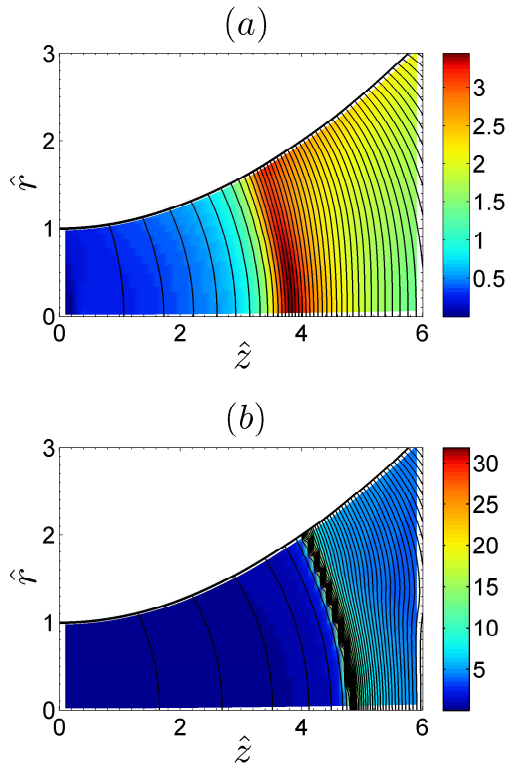


Figure 10: Electric field intensity inside the nozzle,  $eR_S E / T_S$  (background color), and plasma potential isolines. Figure (a) shows a mild QSL, for  $\tau = 9$  and  $\alpha_S = 0.2$ . Figure (b) presents a much more intense QSL, for  $\tau = 18$  and  $\alpha_S = 0.09$ .

licate the relative potential fall along the nozzle. This outstanding result claims that three-species plasmas can bring important benefits, in terms of higher propulsive performances. A minor decrease in potential fall is registered for  $\alpha_S$  too small. This is due to the QSL taking place outside of the nozzle, which would otherwise increase this fall as for higher  $\alpha_S$ .

The plasma total momentum flux along the nozzle at  $z = \text{const}$  sections,  $F(z)$ , can be separated into its ion/momentum and electron/pressure contributions, i.e.,

$$F(z) = F_i(z) + F_e(z), \quad (32)$$

with

$$F_i = \int_{A(z)} m_i n u_i^2 dA, \quad F_e = \int_{A(z)} (n_c T_c + n_h T_h) dA. \quad (33)$$

As the magnetic nozzle transforms internal plasma energy into kinetic energy, ion/momentum thrust increases while electron/pressure thrust decreases. Fig. 11 depicts this thrust development, comparing a two-species plasma with diverse three-species ones. As it can be seen, the hot electron tail causes a large increase in ion/momentum thrust at the location of the QSL, becoming more than two times larger in certain cases. The total plasma momentum also increases with respect to the reference, two-species plasma, although this increase is not concentrated at any particular position. The differences between the profiles of the total momentum for different values of  $\alpha_S$  are smaller than for the ion momentum. This is due to the electron/pressure contribution to the total momentum, which registers a large fall

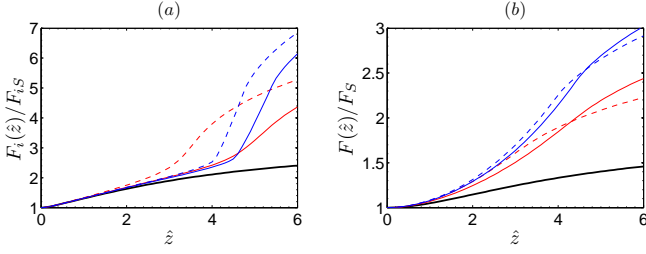


Figure 11: Ion and total plasma momentum evolution along the nozzle at  $z = \text{const}$  sections. Thick black lines are the reference two-species plasma. Red lines denote  $\tau = 9$  (with  $\alpha_S = 0.1$  for the solid line, and  $\alpha_S = 0.2$  for the dashed line). Blue lines indicate  $\tau = 18$  (with  $\alpha_S = 0.07$  for the solid line, and  $\alpha_S = 0.09$  for the dashed line).

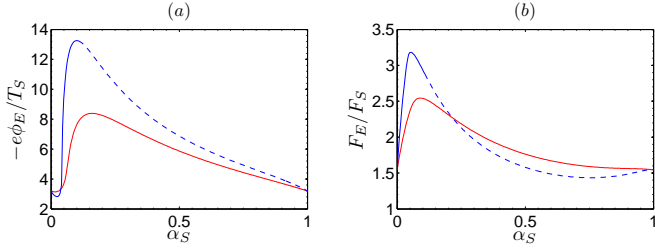


Figure 12: Potential fall along the nozzle (a), and thrust ratio between the final ( $E$ ) and throat ( $S$ ) sections. Red lines correspond to  $\tau = 9$ , blue lines to  $\tau = 18$ . The solution in the CFDL region has been plotted with dashed line, since not every  $\alpha_S$  in this region is feasible in practice.

at the QSL position, compensating for the increase in ion/momentum thrust.

The ratio of thrust between stations  $S$  and  $E$  is defined as  $F_E/F_S$ , which coincides with the ratio of the specific impulse to  $F_S/\dot{m}_i$  — i.e., the specific impulse that would be obtained if no nozzle existed. These two factors are independent of the plasma internal energy at the throat, but depend largely on the nozzle expansion area ( $\varepsilon = A_E/A_S$ , whose influence was already analyzed in [12] and will not be discussed here) and the electron population parameters  $\tau$ ,  $\alpha_S$ . Fig. 12 presents this dependence side by side with the potential fall at the nozzle exit,  $R_E = 3.15$  ( $\varepsilon = 9.92$ ). As it can be seen, the thrust ratio presents a maximum for values of  $\alpha_S$  around 0.1, where it more than doubles for  $\tau = 18$  with respect to the 2-species plasma thrust ratio. For this  $\tau$ , the solution has been continued with a dashed line beyond  $\alpha_{S1}$ , where a CFDL discontinuity forms, although — as shown in Fig. 1 — some of the higher  $\alpha_S$  may not be feasible in a real case for any  $\alpha_0$ .

The nozzle (or plume) efficiency  $\eta_{plume}$  reflects the amount of kinetic energy that is wasted in radial losses, and it is one of the factors contributing to thrust efficiency of the whole thruster. Defined at each  $z = \text{const}$  section, its expression is:

$$\eta_{plume}(z) = \frac{P_{zi}(z)}{P_i(z)} \simeq \frac{F_i^2(z)}{2\dot{m}_i P_i(z)} \quad (34)$$

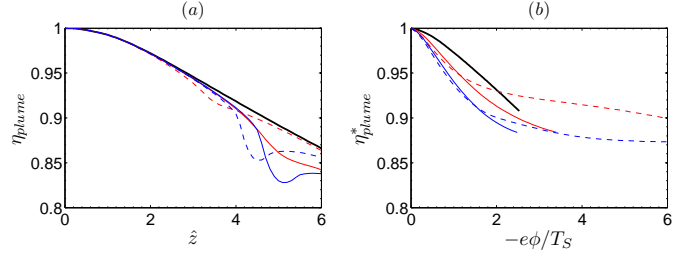


Figure 13: Plume efficiency obtained with the magnetic nozzle for different plasmas. Figure (a) presents this value on  $z$ -constant surfaces. Figure (b) displays the value of  $\eta_{plume}$  on  $\phi$ -constant surfaces, denoted by  $\eta_{plume}^*$ . Thick black lines show the reference, two-species plasma case. Red lines correspond to  $\tau = 9$  (solid:  $\alpha_S = 0.1$ , dashed:  $\alpha_S = 0.2$ ), and blue lines to  $\tau = 18$  (solid:  $\alpha_S = 0.07$ , dashed:  $\alpha_S = 0.09$ ).

with the axial and total ion kinetic powers defined as

$$P_{zi}(z) = \int_{A(z)} \frac{1}{2} m_i n u_{zi}^3 dA,$$

$$P_i(z) = \int_{A(z)} \frac{1}{2} m_i n u_i^2 u_{zi} dA. \quad (35)$$

In [12] it was shown that a nozzle with small diverging rate, and a low ion magnetization plasma provide higher  $\eta_{plume}$ . We focus here on the influence of the EEDF on this efficiency. Simulation results presented on Fig. 13 point out that no relevant change in plume efficiency occurs. However, a sensible decrease in  $\eta_{plume}$  with respect to the two-species plasma case is found locally around the QSL, which is afterward recovered. In some cases ( $\tau = 18$  for instance),  $\eta_{plume}$  reaches a minimum, after which it increases again for a while. This apparently surprising result can be explained if we consider the 2D structure of the plasma expansion: as we saw in Fig. 10, the QSL takes place along a slightly curved line, and not at  $z = \text{const}$ . When ions cross this line, they experience a large acceleration, and due to its curved shape, ions near the outer border are accelerated first, and acquire a strong radial component. This affects the overall efficiency at that  $z = \text{const}$  section, lowering it. Some distance downstream, centerline ions cross the QSL, gaining a large axial velocity, which compensates for this decrease, and (temporarily) rises the value of  $\eta_{plume}$  again.

To account for the 2D geometry of the problem in hand, we shall also define the plume efficiency at  $\phi$ -constant surfaces,  $\eta_{plume}^*$ :

$$\eta_{plume}^*(\phi) = \frac{P_{zi}^*(\phi)}{P_i^*(\phi)}, \quad (36)$$

where

$$P_{zi}^*(\phi) = \int_{A(\phi)} \frac{1}{2} m_i n u_{zi}^2 \mathbf{u}_i \cdot \mathbf{n} dA,$$

$$P_i^*(\phi) = \int_{A(\phi)} \frac{1}{2} m_i n u_i^2 \mathbf{u}_i \cdot \mathbf{n} dA. \quad (37)$$

The graph of Fig. 13 (b) presents the value of  $\eta_{plume}^*$  at constant- $(e\phi/T_S)$  surfaces. As it can be seen, now the efficiency decreases monotonically. Notice that, since each

simulation reaches a different final value of the potential,  $\phi_E$ , each line ends at a different abscissa. From this figure, some conclusions can be drawn about the actual behavior of the plume efficiency in terms of  $\tau$  and  $\alpha_S$ . First of all, the presence of a hot electron tail causes a minor negative effect on the efficiency, slightly increasing radial losses. This effect seems to be more pronounced for higher  $\tau$ . With respect to the influence of  $\alpha_S$ ,  $\eta_{plume}^*$  is maximal for  $\alpha_S = 0$  (two-species plasma). As  $\alpha_S$  increases from 0, this efficiency starts to decrease and soon reaches a minimum. For higher values of  $\alpha_S$ , the efficiency slowly increases again, until both lines for  $\alpha_S = 1$  and  $\alpha_S = 0$  coincide.

## 5 Conclusions

In this paper, we have studied the role of a bi-modal electron energy distribution function, consisting on two hot and cold electron populations, on the plasma expansion through a divergent magnetic nozzle. The 1D model presented in [9, 10] has been used to characterize the three-species plasma flow, and discuss the appearance of quasineutral steepening layer in the plasma magnitudes. This special flow feature can coalesce into a non-neutral double layer, depending on the value of the electron species parameters that define the EEDF: the electron temperature ratio  $\tau$ , and the upstream density ratio  $\alpha_0$ .

The 2D structure of the jet has been analyzed employing the 2D model and the DiMagNo simulation code that we introduced in [12], which has been extended here to include more than one electron species. Simulations reveal the curved shape of the  $\phi$ -constant lines, and that the maximal  $E$  field line does not coincide with them.

We have seen that a small hot electron tail can induce vast benefits on the propulsive performances of the magnetic nozzle. The relative thrust and specific impulse can more than double if the temperature and density ratios are adequate (high  $\tau$ , and  $\alpha_0 \simeq 5\%$ ). However, the plume efficiency,  $\eta_{plume}$ , suffers a minor decrease, which is nevertheless outweighed by the increased total potential fall that the three-species plasma cause.

Finally, all the analysis leads us to conclude that the gains are due to the increased potential fall caused by the anomalous thermodynamics — characterized by an effective specific heat ratio  $\gamma$  lower than 1, meaning that the plasma temperature rises as it expands. Whether it occurs in a quasineutral steepening layer or a double layer is marginal to the plasma response. Actually, the difference between both is a matter of scale only. The double layer formation has no role in the propulsion gain, it is only another consequence of these thermodynamics.

## Acknowledgments

This work was financed by Gobierno de España (Plan Nacional de I+D, Project ESP2007-62694) and the European Community (7th Framework Programme, Grant 218862).

## References

- [1] A. Gurevich, L. Pariiskaya, and L. Pitaevskii, Soviet Physics JETP **22**, 449 (1966).
- [2] S. A. Andersen, V. O. Jensen, P. Nielsen, and N. D'Angelo, Phys. Fluids **12**, 557 (1969).
- [3] R. T. S. Chen and N. Hershkowitz, Physical Review Letters **80**, 4677 (1998).
- [4] C. Charles and R. Boswell, Applied Physics Letters **82**, 1356 (2003).
- [5] O. Batishchev, IEEE Transaction on Plasma Science **37**, 1563 (2009).
- [6] T. Ziemba, J. Carscadden, et al., High Power Helicon Thruster, in *41th Joint Propulsion Conference, Tucson, AR*, AIAA 2005-4119, AIAA, Washington DC, 2005.
- [7] D. Pavarin, F. Ferri, et al., Design of 50W Helicon Plasma Thruster, in *31th International Electric Propulsion Conference, Ann Arbor, Michigan, USA*, IEPC 2009-205, Electric Rocket Propulsion Society, Fairview Park, OH, 2009.
- [8] C. Charles and R. Boswell, Physics of Plasmas **11**, 1706 (2004).
- [9] E. Ahedo and M. Martínez-Sánchez, The Role Of Current-Free Double-Layers In Plasma Propulsion, in *44th Joint Propulsion Conference, Hartford, CT*, AIAA 2008-5005, AIAA, Washington DC, 2008.
- [10] E. Ahedo and M. Martínez-Sánchez, Physical Review Letters **103**, 135002 (2009).
- [11] G. Hairapetian and R. L. Stenzel, Physics of Fluids B **3**, 899 (1991).
- [12] E. Ahedo and M. Merino, Two-dimensional super-sonic plasma acceleration in a magnetic nozzle, submitted to Phys. Plasmas .
- [13] B. Bezzerides, D. W. Forslund, and E. L. Lindman, Phys Fluids **21**, 2179 (1978).
- [14] E. Ahedo and M. Merino, Two-dimensional plasma acceleration in a divergent magnetic nozzle, in *44th Joint Propulsion Conference, Hartford, CT*, AIAA 2009-5361, AIAA, Washington DC, 2008.
- [15] E. Ahedo and M. Merino, Acceleration of a focused plasma jet in a divergent magnetic nozzle, in *31th International Electric Propulsion Conference, Ann Arbor, Michigan, USA*, IEPC 2009-002, Electric Rocket Propulsion Society, Fairview Park, OH, 2009.
- [16] M. Zucrow and J. Hoffman, *Gas dynamics*, Wiley, New York, 1976.
- [17] J. Jackson, *Classical Electrodynamics*, Wiley, New York, 1999.
- [18] M. Abramowitz and I. Stegun, *Handbook of Mathematical Functions*, Dover, New York, 1965.